Chaos, Solitons and Fractals 136 (2020) 109807

Contents lists available at ScienceDirect

Chaos, Solitons and Fractals

Nonlinear Science, and Nonequilibrium and Complex Phenomena

journal homepage: www.elsevier.com/locate/chaos

Steel corrosion prediction based on support vector machines

Ya-jun Lv[a,b], Jun-wei Wang[c], Julian Wang[d], Cheng Xiong[a,b], Liang Zou[a,b], Ly Li[a,b], Da-wang Li[a,b,*]

[a] Department of Civil and Transportation Engineering, Shenzhen University, Shenzhen 518060, China
[b] Guangdong Province Key Laboratory of Durability for Marine Civil Engineering, Shenzhen 518060, China
[c] Department of Civil and Architectural Engineering, Henan University of Technology, Zhengzhou 450001, China
[d] Department of Architectural Engineering, Pennsylvania State University, University Park, PA 16802, United States

ARTICLE INFO

Article history:
Received 5 March 2020
Revised 2 April 2020
Accepted 6 April 2020
Available online 27 April 2020

Keywords:
Corroded steel
SVM
Sectional corrosion rate
Image recognition
Prediction model

ABSTRACT

In this paper, the 3D coordinate data of the corrosion condition of rebar are obtained by a 3D scanning method. Seven numerical parameters, such as the roundness, the section roughness, the inscribed circle radius/circumscribed circle radius and the eccentricity, are obtained by the numerical calculation method. These seven parameters are used to characterize the cross-section morphology of rusted steel bars. The particle swarm optimization support vector machine (PSO-SVM) and the grid search support vector machine (GS-SVM) are used to calculate these seven cross-section digitization parameters to predict the sectional corrosion rate of steel. This work concluded that these two optimization support vector machine (SVM) methods can accurately predict the sectional corrosion rate of steel. Compared with the GS-SVM model, the PSO-SVM steel corrosion prediction model is more accurate.

1. Introduction

After steel bars are embedded in concrete, both the internal and external environment of the concrete will changed [1], which will cause corrosion of the reinforcement. The mechanical properties of the steel bars will decrease due to the reduction of the cross-section, and the strength and ductility of the steel bars will also be reduced [2,3], thereby reducing the bearing capacity and durability of the concrete structures [4,5].

To evaluate the shape, bearing capacity and durability of the corroded steel bar to reflect the true corrosion condition of the steel bar, scholars have conducted research on the quantitative evaluation of the corrosion condition of steel bars. The quality corrosion rate is a parameter often used by scholars. Scholars often use the weighing method to determine the quality corrosion rate of steel bars [6-8], but the quality corrosion rate is a relatively rough measure that can only measure the average corrosion of steel bars. The minimum section of the steel bar cannot be clearly reflected [9], and at the same time, it cannot characterize the detailed features of the rusted bar shape. Stewart and Al-Harthy [10] used a Vernier caliper to test the geometrical characteristics of the corroded steel section and obtained the position and size of the minimum cross-sectional area. Du et al. [3,11] vertically placed the corroded steel bars into an overflow container and used the drainage method to measure the volume of the overflowing water along the axial direction of the corrosion rate distribution. Zhu et al. [12,13] used a slicing method to cut corroded steel bars into sections and obtained the rust rate distribution by measuring the weight of the segmented steel sheets. However, the above test methods still have some limitations, there are certain errors in the data measurement, and it is difficult to accurately analyze the cross-sectional shape characteristics of the corroded steel bar. Zhao et al. [14] used low-field nuclear magnetic resonance (LF-NMR) imaging to investigate moisture transport in cement-based materials (CBMs) considering the influences of the water/binder (w/b) ratio. With the advancement of technology, scholars use X-ray computed tomography (XCT), 3D scanning, and other methods to determine the shape of corroded steel bars. Basically, these test methods may reflect the potential corrosion of steel bars. Li et al. [15,16] used a 3D scanning method to measure the corroded steel bar, obtained the three-dimensional coordinate data of the corroded steel surface, and analyzed the extracted data; they found that the pit depth, the residual cross-sectional area and the minimum moment of inertia of the steel bars after rusting follow a variety of probability distributions, and the correlation between the pit depth and the mass loss is weak. Cheng et al. [17] used Computed Tomography (CT) technology to detect and measure the corrosion of steel bars. Sriramadasu et al. [18] used ultrasonic scatter-

* Corresponding author at: Department of Civil and Transportation Engineering, Shenzhen University, Shenzhen 518060, China.
E-mail address: lidw@szu.edu.cn (D.-w. Li).

https://doi.org/10.1016/j.chaos.2020.109807
0960-0779/

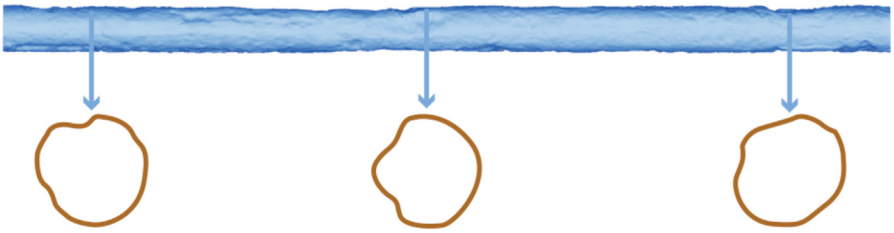

Fig. 1. Different sectional shapes of a corroded bar in different positions.

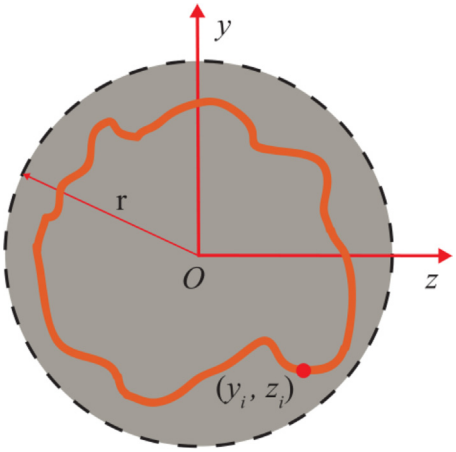

Fig. 2. Corrosion condition of a section of rusted rebar.

ing techniques to measure corroded steel bars, which can identify pitting corrosion. Dinh et al. [19,20] proposed an image processing technique based on the automatic detection and localization algorithm of ground-penetrating radar (GPR) data to identify potential steel corrosion peaks. Dong et al. [21] proposed the XCT imaging method for tracking and analyzing the evolution of steel corrosion in concrete. This detection method is very accurate, and the cross-sectional shape of the corroded steel bar can be extracted and digitized. Common test methods are mass method, vernier caliper method, drainage method, XCT test method and 3D scanning method. Compared with the mass method, vernier caliper method, and drainage method, the 3D scanning method not only has better test accuracy and test efficiency, but also can reflect the details of the corroded steel bars tested. Compared with the high-precision XCT method, the 3D scanning method has low cost, high efficiency, and more accurate test results. However, during the test, it is necessary to remove the concrete outside the steel bar and clean the corroded steel bar.

Compared to the above test methods for the corrosion rate of steel bars, this study concentrates on a unique perspective of predicting the corrosion rate of the steel. The motivation of conducting this research is the fact that most existing buildings (especially the aged building) may not have the detailed design document (i.e., rebar sizes) of the original concrete structures. In such situations, although the current 3D scanning techniques are capable to accurately record and detect the current corrosion conditions of the corroded steel rebars, the accurate sectional corrosion rate (the loss over the initial condition) is still not able to be obtained. These accurate corrosion rate values are more crucial than the current corrosion status to determine or estimate the mechanical performance of the steel bars and associated concretes. Therefore, a predictive method is needed to address this challenge – attaining the sectional corrosion rate for existing building structures without knowing the original design parameters. A variety of predictive modeling studies have indicated that Back Propagation(BP) neural networks, SVM, random forest methods, and other algorithms can train data and build models, and predict unknown data with strong operability and high accuracy [22-24]. Xue and Cui [25] used a BP neural network to repair images, which improved the image details and edge recognition and greatly improved image quality. Zhi and Lui [26] built a face recognition model based on principal component analysis, a genetic algorithm and a SVM that can achieve personal identity authentication well; genetic algorithms can also be used for various characterization and fire prediction applications. The accuracy of genetic algorithms is reliable, the results are more accurate, and they have a high reference value [27,28]. Bousselham et al. [29] used genetic algorithms to solve the inverse problem. This method can be used for brain tumor screening and can be implemented on a graphics processing unit (GPU), which greatly accelerates the speed of reverse recognition in genetic algorithms. Cai et al. [30] designed a parallel genetic algorithm and proposed an image-based detection algorithm strategy which can effectively improve the quality of automatic crane hoisting path planning in complex environments. Using a SVM model for image analysis and judgment can improve the accuracy of recognition and provide a better data reference, which can be applied to many fields [31-33]. Gong et al. [34] used a random forest model to estimate the roughness index of flexible pavement. The parameters included the road traffic, the maintenance status, the structural form, and the local climate characteristics. In total, 11,000 data samples were collected, of which 80% of the sample was used to train the model, and the 20% sample was used to test the prediction model. The resulting model has high accuracy. Intelligent algorithms can be used to train the known data and build models that enable accurate analysis and prediction of unknown data.

In this study, the 3D coordinate data of the corrosion condition and distribution of the reaction steel are obtained by a 3D scanning method. First, to quantify the characteristics of the steel bar's corrosion conditions, we defined seven parameters related to the bar's corroded shapes (e.g., roundness, sectional roughness) Subsequently, a dataset about these seven parameters (independent variables) and the sectional corrosion rate (dependent variable) was obtained through 3D scanning techniques on prepared specimens. Then, we built a SVM prediction model based on two optimization methods using these seven cross-sectional parameters to predict the sectional corrosion rate of steel.

2. Experiment and methods

2.1. Sectional characteristics of corroded steel bar

When a steel bar gets rusted, it may have different sectional corrosion features. As shown in Fig. 1, the 3D record of a corroded steel bar from our previous experiment presents there are significant differences between the different sections. The overall weight (volume) loss rate couldn't reflect the detailed corrosion characteristics in particular sections which may directly determine the final mechanical performance of the corroded steel bars and associated

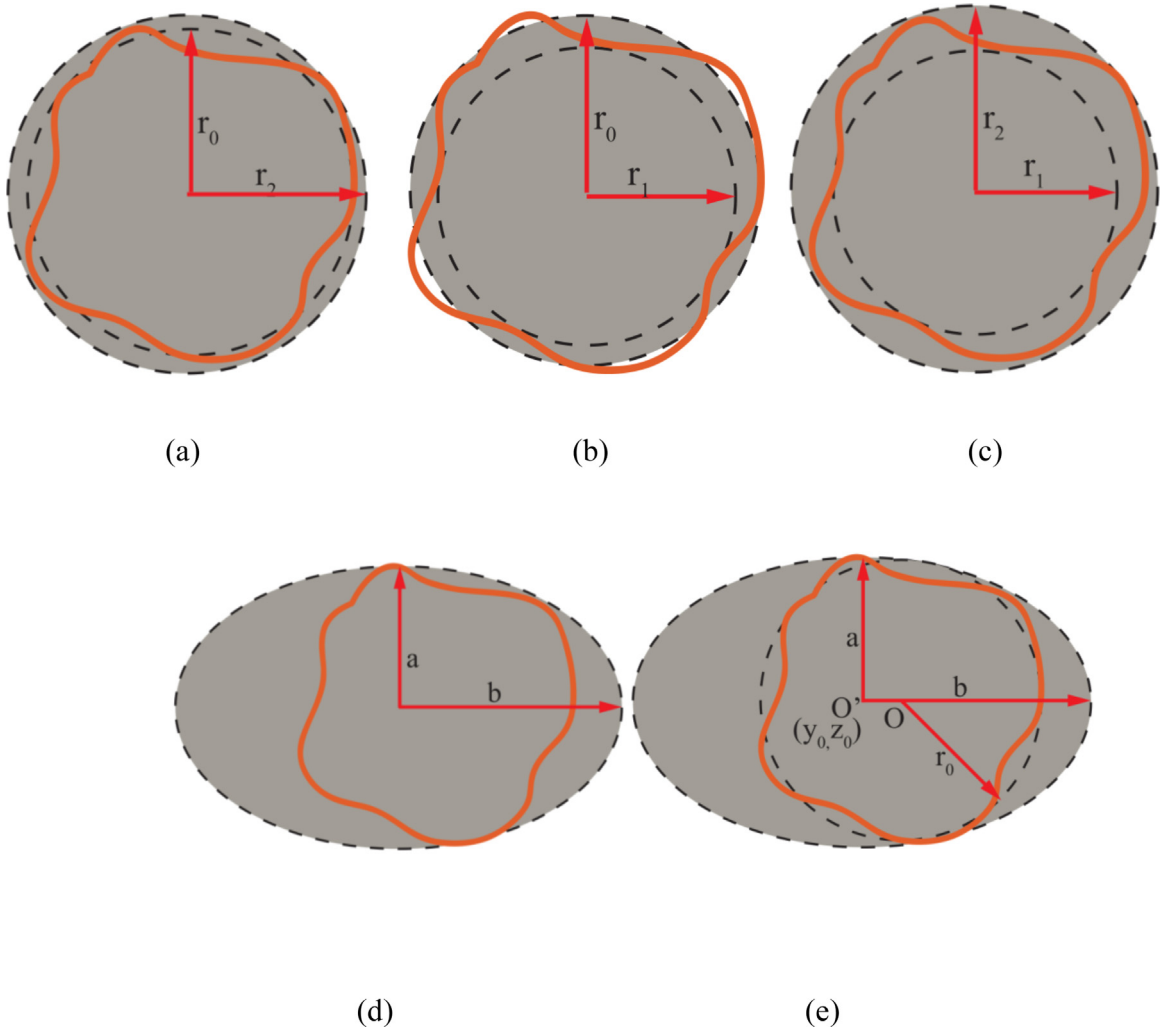

Fig. 3. Diagram of the sectional geometric parameters corroded bar.

concretes. Therefore, in this study, we focused on sectional corrosion rate.

The scan data is the three-dimensional position coordinates of the surface of the reinforcement. The accuracy of these data is 0.1 mm. The center point of the bottom surface of one end of the unreinforced front reinforcing bar is taken as the coordinate origin, where the OX axis is perpendicular to the bottom circular surface, and the OY axis and the OZ axis are parallel to the bottom circular surface. Fig. 2 presents the schematic cross-section of a corroded steel bar. the corrosion rate of steel sections is calculated in Eq. (1).

$$\tau = \frac{A_0 - A_1}{A_0} \times 100\% \tag{1}$$

where A_0 refers to the section area before corrosion with the same original section area; A_1 is the residual section area after corrosion, calculated by integration, as shown in Eq. (2):

$$A_1 = \iint dydz = \frac{1}{2}(ydz - zdy) = \frac{1}{2}\sum_{i=1}^{n}(y_i z_{i+1} - y_{i+1} z_i) \tag{2}$$

where y_i,y_{i+1} is the y-axis coordinate, and z_i,$z_{i+1}$is the z-axis coordinate

Furthermore, as shown in Fig. 3, we obtained the following geometric parameters: r_1 is minimum inscribed circle radius of the section profile, r_2 is maximum circumscribed circle radius of the section profile, r_0 is the radius of the fitting circle of a section profile, a is the short side of the fitting ellipse of a section profile, b is the long side of the fitting ellipse of a section profile, y_0,z_0 is the central coordinate of the fitting ellipse, and p is the perimeter of the residual section of the rusted section.

(a) Diagram of the fitting circle and the circumcircle; (b) Diagram of the fitting circle and the incircle; (c) Diagram of the fitting incircle and the circumcircle; (d) Diagram of the ellipse; (e) Diagram of the incircle and the ellipse.

Upon the above geometric parameters, we defined seven cross-sectional parameters to represent the cross-sectional corrosion features, which include:

- η, the ratio of the radius of the minimum incircle to the radius of the fitting circle,
- δ, the ratio of the radius of the maximum circumcircle to the radius of the fitting circle,
- υ is the ratio of the radius of the minimum incircle to the radius of the maximum circumcircle,
- e is the eccentricity,
- ε is the ratio of short side of the fitting ellipse to long side of the fitting ellipse,
- χ is the roundness;
- γ is the section roughness.

These cross-section features can be obtained by the least squares method via Matlab [33,34]. Eqs. (3)–(9) were used in these

Table 1
Composition of concrete.

Composition	Cement (P42.5)	Fine aggregate	Coarse aggregate	Water	Additives
Wt%	14.6	29.8	48.7	6.7	0.2

Table 2
Composition of the HPB300 Steel Bars.

Element	C	Si	Mn	P	S	Cr	Mo	Ni	Co	Cu	V	Sn	Fe
Wt%	1.10	0.03	0.2	0.07	0.2	0.01	0.07	0.20	0.01	0.20	0.02	0.03	97.45

calculations.

$$\eta = r_1/r_0 \tag{3}$$

$$\delta = r_2/r_0 \tag{4}$$

$$\upsilon = r_1/r_2 \tag{5}$$

$$\mathrm{e} = \left(\sqrt{\mathrm{y_0}^2 + \mathrm{z_0}^2}\right)/r_0 \tag{6}$$

$$\varepsilon = a/b \tag{7}$$

$$\chi = p^2/(4\pi A_1) \tag{8}$$

$$\gamma = A_1/\left(\pi {r_0}^2\right) \tag{9}$$

For the original situation of an unused steel bar, η, δ, υ, ε, and γ equal 1, e equals to 0, and χ is 1 Comparatively, for a corroded steel bar, η, υ, ε, and γ are smaller than 1, δ and χ are larger than 1, and e is larger than 0.

2.2. Preparation of reinforced concrete specimens

First, 400 mm×350 mm×250 mm reinforced concrete specimens were produced. The composition ratio of the concrete is shown in Table 1. Each concrete specimen contains 3 HPB300 steel bars with diameters of 14 mm. The chemical composition of the steel bars is shown in Table 2. The reinforced concrete test specimens were first air cured at a room temperature of approximately 25 °C for 28 days. Different types of concrete, chemical composition and compactness will greatly affect the corrosion of steel bars in concrete. In this study, we use the same type of concrete to ensure that the steel bars rust in the same situation, and to ensure that the steel bars have the same corrosion morphology. This can ensure the consistency of steel bar corrosion.

In the process of making reinforced concrete specimens, first, the rust layer and oxidized material on the surface are removed, and the 75 mm portion of the steel bar is covered with epoxy resin to protect the steel bars at the ends. The 250 mm middle portion of the steel bars is corroded, and the test piece is placed in a 5% sodium chloride solution. In this paper, the steel rusting is accelerated by means of electrification. The steel is used as the anode, the external metal (usually stainless steel or copper) is used as the cathode, and a constant current or a constant voltage is applied between the anode and the cathode. Introducing chloride ions from the external solution into the concrete causes the corrosion of the steel bars [15,35].

2.3. 3D scanning of corroded bars

After the accelerated corrosion of the steel bar is completed, the concrete test piece is broken, the rusted steel bar is removed and cleaned according to the standard method specified in ASTM G1-03. After cleaning, the surface morphology of the corroded steel bar was measured using a 3D optical scanner with a scanning accuracy of 0.05 mm. The scanning process provided three-dimensional coordinates for each point on the surface of the reinforcing bar. The scanning method was as described in references [2,15]. After 3D scanning, the rusted steel bar image can be accurately obtained. As shown in above Fig. 2, the points in these images are formed by three-dimensional coordinate points. By using the least squares method, the seven defined cross-sectional parameters were obtained via Eqs. (3)–(9) in Matlab. The sectional corrosion rate was also calculated for each selected section. So, a dataset about cross-sectional parameters of corroded steel bars was prepared (the details are described in Section 3.1).

2.4. Theory of the support vector machine (SVM) model

The basic principle of SVMs [36-40] is to map the input sample x on a high-dimensional feature space $\boldsymbol{F}$ via a nonlinear mapping function $\phi(x)$. The linear regression function was created on the principle of the minimization of structural risks [41,42]:

$$y' = A_{sc}(x) = w \cdot \phi(x) + b \tag{10}$$

where w refers to the weight vector, $w \in F$, b is the bias vector, $b \in R$, y' is the predicted value, and y is the measured value.

When solving regression fitting problems by SVMs, fitting errors should be considered and permitted. Relaxation factors were introduced. On the basis of SVMs, a linear insensitive loss function (ε) was introduced to obtain the regression SVM. Therefore, the regression problem was converted into a solution of the objective function for the minimization of structural risks, namely, the values of w and b for the minimization of the objective function.

$$\begin{cases} \min \left\{ \left\{ \frac{1}{2}\|w\|^2 + C\sum_{i=1}^{n}\left(\zeta_i + {\zeta'}_i\right) \right\} \right. \\ s.t. \begin{cases} w \cdot \varphi(x) - y_i + b \le \varepsilon + {\zeta'}_i \\ y_i - w \cdot \varphi(x) - b \le \varepsilon + {\zeta'}_i \\ \zeta_i \ge 0, \ \ {\zeta'}_i \ge 0 \\ i = 1, 2, 3 \cdots n \end{cases} \end{cases} \tag{11}$$

where $C>0$, which is a penalty factor. It controls the penalty degree of each sample beyond error ε. ζ_i and ${\zeta_i}'$ are relaxation factors indicating the upper and lower limits of the sample training errors under the condition of $|y_i - [w \cdot \phi(x) + b]| < \varepsilon$, respectively. ε refers to the linear insensitive loss function:

$$H_\varepsilon(y) = \begin{cases} 0 & |f(x) - y| < \varepsilon \\ |f(x) - y| - \varepsilon & |f(x) - y| \ge \varepsilon \end{cases} \tag{12}$$

Eq. (3) shows that when the absolute error of the predicted and measured values is less than ε, the absolute error would be ignored; otherwise, it will be included in the errors.

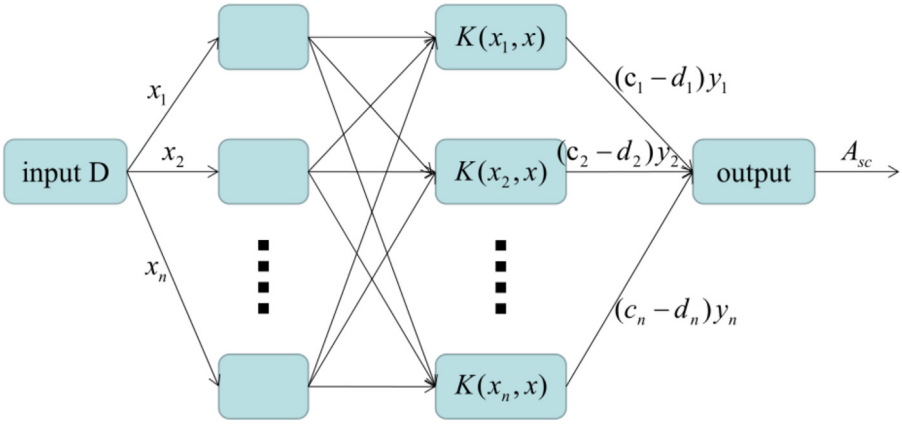

Fig. 4. Diagram of the SVM regression structure.

While solving Eq. (2), Lagrange multipliers c_i and d_i are introduced to construct the Lagrange function. Convex optimization [43] was simplified as a maximization of the quadratic form, and the saddle point of the Lagrange equation was solved. The partial derivative of each variable was determined and set to zero. According to the dual principle, it can be converted into:

$$\begin{cases} \max \begin{cases} \sum_{i=1}^{n} y_i(c_i-d_i) - \frac{1}{2}\sum_{i,j=1}^{n}\left(c_i-c_i'\right)\left(c_j-c_i'\right)\left(x_i-x_j\right) - \\ \varepsilon\sum_{i=1}^{n}\left(c_i+c_i'\right) \end{cases} \\ s.t. \begin{cases} \sum_{i=1}^{n}\left(c_i-c_i'\right)=0 \\ 0\le c_i\le C \\ 0\le c_i'\le C \end{cases} \end{cases} \tag{13}$$

When solving the nonlinear problem by means of an SVM, the input sample x was mapped onto the high-dimensional feature space $\boldsymbol{F}$ via a nonlinear mapping function$\phi(x)$. Then, linear regression of the high-dimensional feature space is performed. Conversion from low-dimensional space to high-dimensional space is realized by $K(x_i,x_j)=\phi(x_i)\cdot\phi(x_j)$ [44]. This function cannot replace dot products in high-dimensional space, avoid solutions of the nonlinear mapping function $\phi(x)$and greatly reduce the computation time and complexity. This paper adoptes a radial basis function (RBF) [45], as shown below:

$$K\left(x_i,x_j\right)=\exp(-\gamma x_i-x_j{}^2) \tag{14}$$

where γ is the nuclear parameter ($\gamma>0$) and x_i-x_j is the Euclidean norm. After introducing the nuclear parameter, the optimization objective can be converted into

$$max\begin{Bmatrix} \sum_{i=1}^{n} y_i(c_i-d_i) - \frac{1}{2}\sum_{i,j=1}^{n}\left(c_i-c_i'\right)\left(c_j-c_i'\right)K\left(x_i,x_j\right) - \\ \varepsilon\sum_{i=1}^{n}\left(c_i+c_i'\right) \end{Bmatrix} \tag{15}$$

$$s.t.\begin{cases} \sum_{i=1}^{n}\left(c_i-c_i'\right)=0 \\ 0\le c_i\le C \\ 0\le c_i'\le C \end{cases}$$

Then, the SVM nonlinear regression function can be solved.

$$A_{sc}(x)=\sum_{i=1}^{n}(c_i-d_i)K\left(x_i,x_j\right)+b \tag{16}$$

The diagram of the regression SVM structure is shown in Fig. 4. In Fig. 4, A_{sc}, the output sectional corrosion rate is a linear combination of intermediate nodes. Each intermediate node corresponded to one support vector. x_1, x_2, $x_3\cdots$, x_n are input variables and c_i-d_i is network weight.

2.5. Support vector machine optimization algorithm

2.5.1. PSO algorithm

To create an accurate nonlinear SVM regression prediction model, the values of the penalty factor C and the nuclear parameter g should be determined. Reasonable selection and optimization of algorithms are very important for finding the optimum parameters of the SVM. In 1995, Kennedy and Eberhaert proposed the PSO algorithm, which could optimize the penalty factor C and the kernel parameter g, and was characterized by the simple principle, required only a few calculation parameters, performed quick searches and had a high efficiency [40,46,47]. This algorithm can show the dynamic particle tracking of the current search status

Table 3
Basic information of the prepared dataset.

Geometrical characteristics	Min	Max	Average	Standard deviation
r_1/r_0	0.46934717	0.96415378	0.836540327	0.110293523
r_2/r_0	1.02536834	1.56266562	1.159350838	0.128104486
r_1/r_2	0.69004853	0.92745803	0.799415107	0.047937949
Eccentricity	0.00157042	0.52769594	0.127400673	0.12939563
a/b	0.87755515	0.99730070	0.956720719	0.023610318
Roundness	0.97880106	1.38956400	1.041947542	0.050982564
Section Roughness	0.96842186	1.011217775	0.9877116	0.00651862
Corrosion rate of steel section	0.000756424	0.163595305	0.071521198	0.039892237

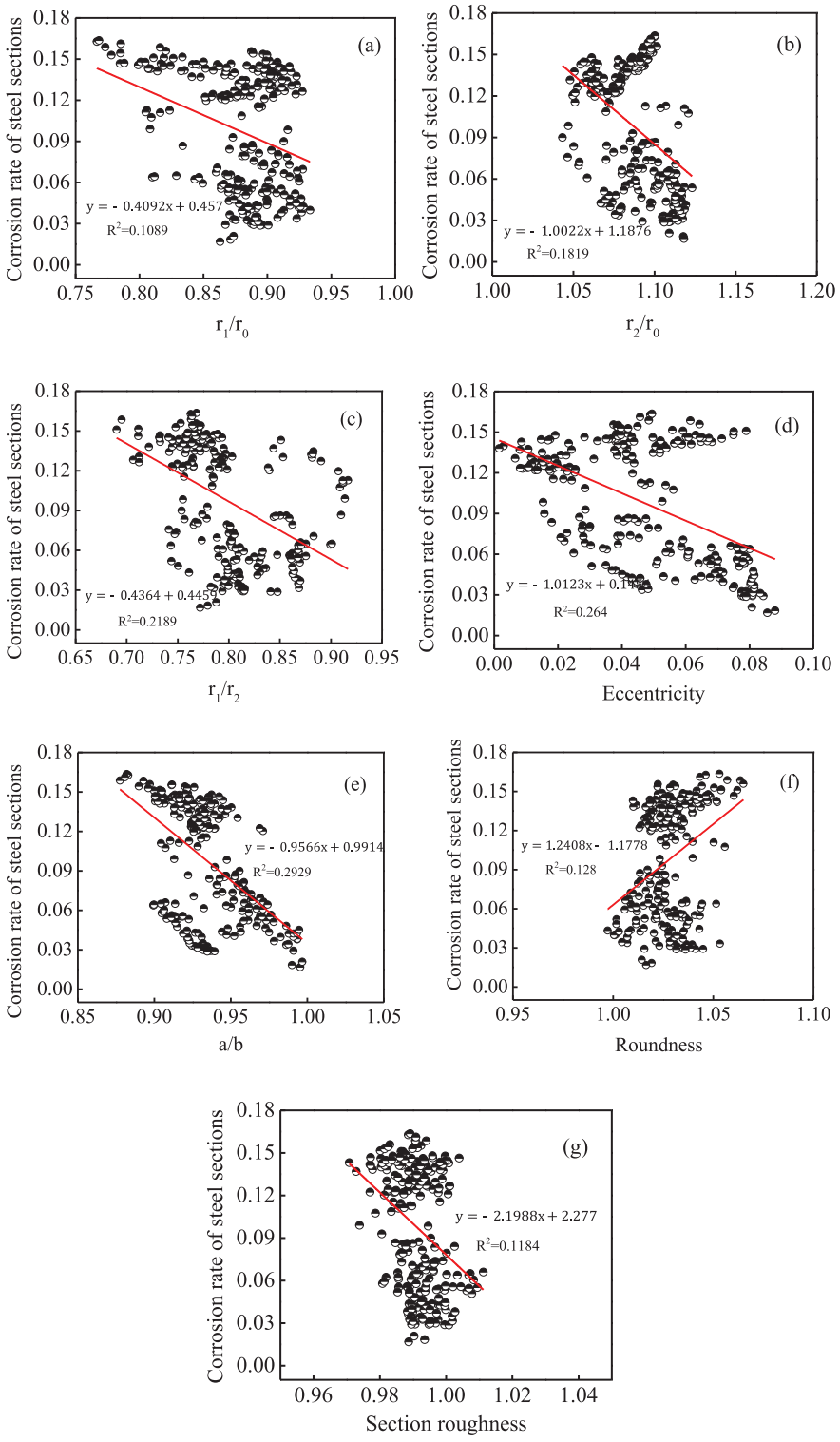

Fig. 5. Relationship between the corrosion rate and the defined geometric parameters.

and adjust the search strategy to achieve the optimal search (see the references for details on the algorithm) [46, 48-50].

The steps for optimizing the penalty factor C and the nuclear parameter g by the PSO algorithm are as follows:

(1) Initialization: Randomly generate the velocity and position of the particles, set the learning factors c_1 and c_2, and obtain the penalty factor C and the kernel parameter g.

(2) Fitness evaluation: Calculate the fitness function value of each particle, and initialize the local optimal value and the global optimal value.

(3) Renewal process: Update the velocity and position of the particle to generate a new population, compare the fitness value with its own historical optimal value, and update the global optimal values of the population parameters C and g.

(4) Stop condition: When the maximum generation is reached, the optimization stops and the optimum C and g are output.

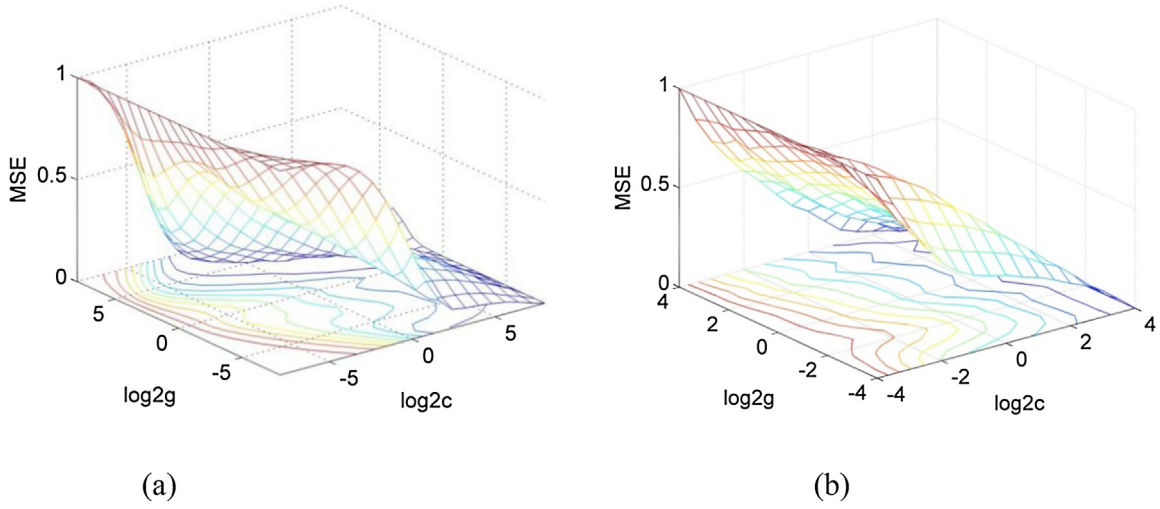

Fig. 6. 3D views of the GS optimization, (a) Optimization within a large scope, (b) Optimization within a small scope.

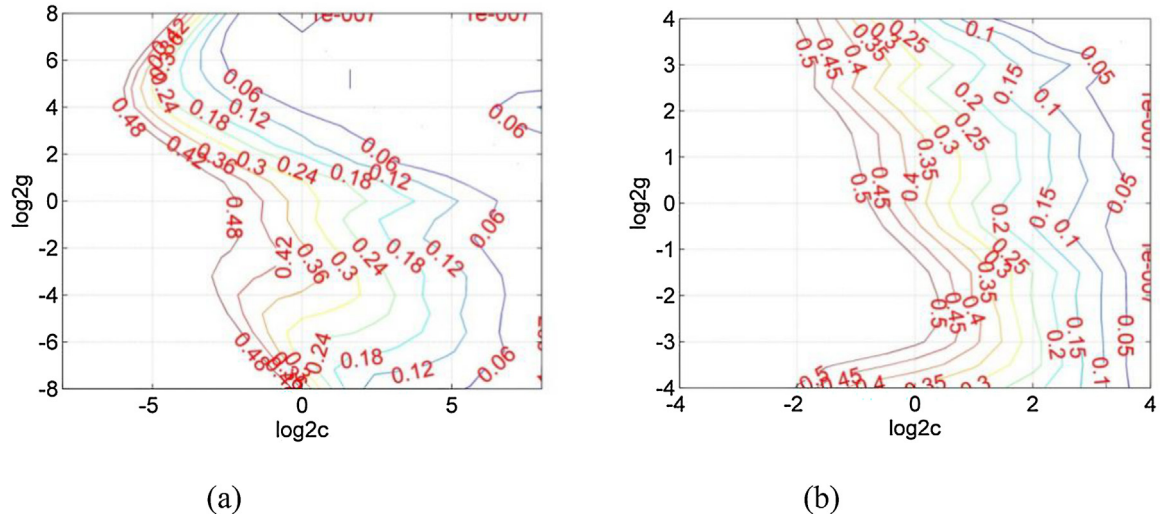

Fig. 7. Contour map of the GS optimization, (a) Optimization within a large scope, (b) Optimization within a small scope.

2.5.2. Grid search (GS) algorithm

The basic principle of optimization via grid search is to conduct optimization within a large scope first and then within a narrowed scope. The values of C and *g* were selected in a certain grid. Training sets for C and *g* were obtained by K-CV cross validation to verify the accuracy rate of the classification. Finally, the C in the training set with the highest accuracy rate was selected as the optimal parameter [51].

2.5.3. Evaluation indexes of the prediction model

MRE, MAE, RMSE, R^2 and MSE were employed to evaluate the performance and prediction effects of the SVM model [52]. The MRE reflects the departure degree of the predicted value, the MAE shows the real error of the predicted value, the RMSE measures the deviation between the predicted value and the real value, and MSE reflects the difference between the real value and the predicted value [53-55]. For these indexes, value approaching zero indicate a small error. R^2 measures the fitting degree of a model, where a value approaching one indicate a good fit.

$$MRE = \frac{|y_i' - y_i|}{ny_i} \tag{17}$$

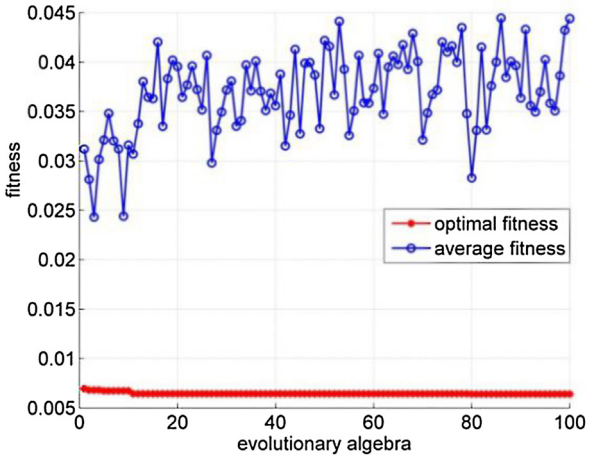

Fig. 8. PSO optimization.

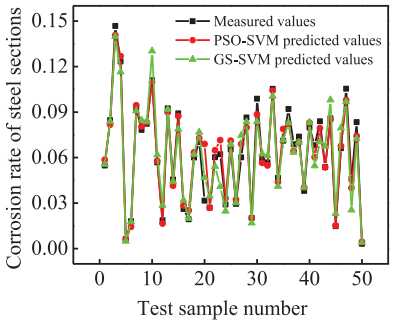

Fig. 9. Prediction results of the testing sample.

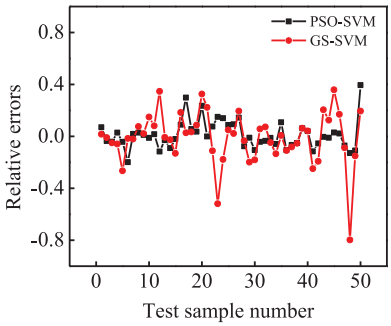

Fig. 10. Relative error between the predicted value and the measured value.

$$MAE = \frac{1}{n}\sum_{i=1}^{n}\left|y_i' - y_i\right| \tag{18}$$

$$RMSE = \sqrt{\frac{\sum_{i=1}^{n}(y_i' - y_i)^2}{n}} \tag{19}$$

$$R^2 = \frac{\sum_{i=1}^{n}(y_i' - \overline{y_i})^2}{\sum_{i=1}^{n}(y_i - \overline{y_i})} \tag{20}$$

$$MSE = \frac{\sum_{i=1}^{n}(y_i' - y_i)^2}{n} \tag{21}$$

where y_i' refers to the predicted value, y_i is the real value, and $\overline{y_i}$ is the mean of real value (i=1,2,...,n)

3. Results and discussion

3.1. Correlation analysis of the section characteristics and the corrosion rate of a rebar section

In this study, the authors attempt to establish the relationship between the corrosion rate and the geometry of the steel sections. The basic dataset information is shown in Table 3. In Section 2.3, we define seven geometric parameters based on the cross-sectional shape of the corroded steel, as shown in Eqs. (3)–(9). The relationship between the corrosion rate of the steel section and the seven geometric parameters is shown in Fig. 5. According to the figure, the related coefficients (R^2) were between 0.1089 and 0.2929, and the correlation between a single geometric parameter and the section corrosion rate is very weak, indicating that it is difficult to predict the section corrosion rate of steel bars by a single geometric parameter because the corrosion of rebar sections is not determined by a single geometric factor but by multiple factors. As a result, the prediction of rebar corrosion via a steel geometric bar can be transformed into a high-dimensional nonlinear problem, which is very suitable for solving with a support vector machine.

3.2. Analysis of the prediction results from the SVM model

3.2.1. Analysis of the parameter optimization

The penalty factor C and the kernel parameter g are a low-fitness combination of the optimization algorithm. To compare the effects of parameter optimization, K-fold cross validation (K-CV) is applied to the training sets. Optimization of C and g is conducted by a grid search (GS) and particle swarm optimization (PSO), respectively. For GS optimization, rough optimization is conducted first to determine the optimum parameter, and then fine optimization is conducted to choose the parameters, where both C and g are within $[2^{-8}, 2^8]$ with a step interval of 0.5. Fig. 6(a) is a 3D picture of the cross-validation of C and g within $[2^{-8}, 2^8]$. Fig. 7(a) is a picture of cross-validation and then further narrows the optimization range. Figs. 6(b) and 7(b) are the 3D pictures of the cross-validation of C and g within $[2^{-4}, 2^4]$ and a 2D picture of cross-validation, respectively, where the x-axis, y-axis and z-axis indicate the RBF kernel parameter, the penalty factor C and the mean square error MSE, respectively. The optimization scope is gradually narrowed down to obtain the optimal parameter combination. By GS optimization, when the MSE reaches its minimum value, then $C = 5.6569$ and $g = 16$.

By PSO optimization, the initial parameters are set up as the following: Q=20, $E = 100$, c_1=1.4 and c_2=1.6. According to Fig. 8, after 100 iterations, the optimum fitness is gradually obtained from the average fitness to obtain the optimal parameter combination. In the process of selecting the optimum parameters, the MSE is selected to evaluate the parameters. When the MSE reaches its minimum value, then $C = 1.998$ and g=51.096.

3.2.2. Analysis of the prediction results

In this study, the GS-SVM and PSO-SVM models are used to train and predict the data in the sample set. In this study, 1050 corroded steel cross-section data are selected, from which 1000 data points are randomly chosen as the training set. After training with the training set, the remaining 50 rebar sections formed the testing set, and its prediction results are shown in Fig. 9. To assess the accuracy of the prediction results of both models, the MRE, MAE, RMSE, R^2, and MSE are selected. The prediction results of the testing samples for both the PSO-SVM and GS-SVM models are shown in Fig. 11, and their fractional errors are shown in Fig. 10. According to these figures, the MRE, MAE, RMSE and MSE values are low in both models, and the R^2 values of both models are greater than 0.9, indicating that both models may be applied to the evaluation of the sectional corrosion rates of steel bars. Hence, both models can be used to correctly predict sectional corrosion rates of steel bars according to the parameters of the corroded bar.

According to Fig. 9, the maximum relative errors of the PSO-SVM and GS-SVM models are 0.394329 and −0.797804, respectively, and their minimum relative errors are −0.000731 and −0.007548, respectively. Both the maximum and minimum relative errors of the PSO-SVM model are less than those of the GS-SVM model, showing that the PSO-SVM model has a higher prediction precision. According to Figs. 11 and 12, the values of the MRE, MAE, RMSE, and MSE of the PSO-SVM model are smaller than those of the GS-SVM model and its R^2 is close to 1, indicating high prediction precision, good fitness, and performance. In the PSO-SVM algorithm, all particles adjust their speed and position according to the current single extreme value they find and the current global optimal solution shared by the entire particle swarm to obtain the optimal solution, which has advantages in the prediction of more sample data. Grid search algorithm is a practical data search method, which is suitable for searching multi-dimensional arrays in parallel from different growth directions at the same time. The

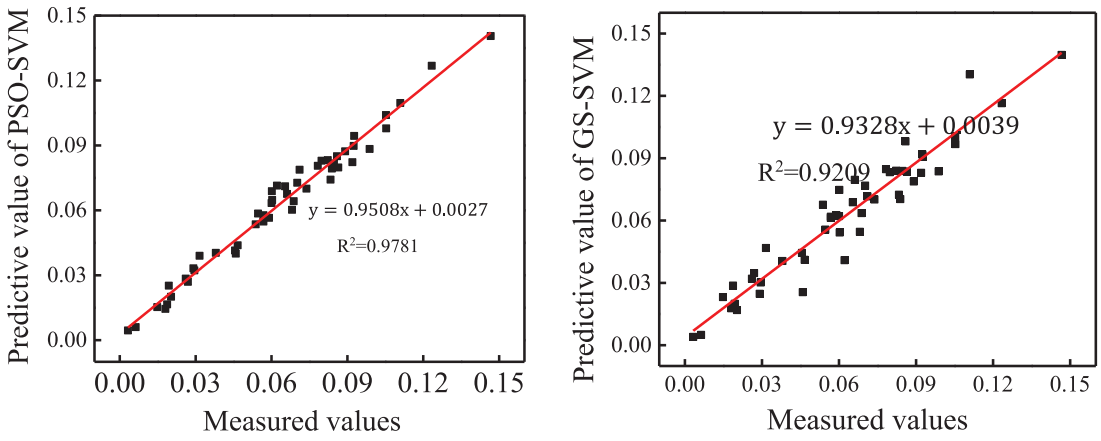

Fig. 11. Relations between the predicted value and the actual (measured) value.

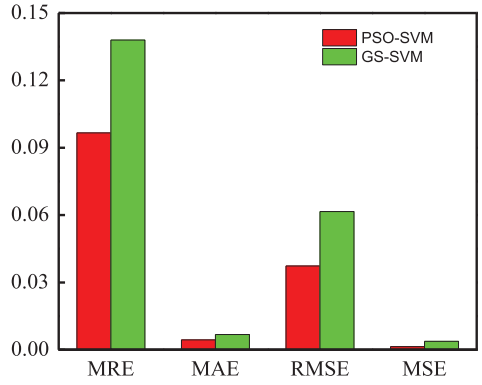

Fig. 12. Indexes for the evaluation of the average prediction effects.

grid search method is to search for a combination of parameters to obtain the best parameters, which has advantages in the prediction of smaller sample data. The sample data in this article is large, and PSO-SVM is more suitable for the data situation in this case.

4. Conclusion

In this work, we quantified the characteristics of sections of corroded bars and then established a comprehensive corrosion rate model of rebar sections by the PSO-SVM and GS-SVM models. The developed comprehensive corrosion rate model involves seven parameters, namely, the ratio of the radius of the smallest incircle to the radius of the fitting circle (η), the ratio of the radius of the largest circumcircle to the radius of the fitting circle (δ), the ratio of the radius of the smallest incircle to the radius of the largest circumcircle (υ), the eccentricity (e), the ratio of the short side of the fitting ellipse to the long side of the fitting ellipse (ε), the roundness (χ) and the section roughness (γ) to characterize section features of the corroded bar. The testing results demonstrated that the prediction of the rebar section corrosion rates models using the two methods PSO-SVM and GS-SVM are very accurate (R^2>0.9). Comparatively, the section corrosion rates prediction accuracy of the PSO-SVM model (R^2=0.98) is slightly higher than the accuracy of the GS-SVM model (R^2=0.92). Additional, to validate and further implement this predictive method, the other types of concrete structures with different steel bars would be investigated by following the procedure and method established in this paper. The purpose of this study is to propose a method for predicting cross-section corrosion rate using SVM. The influence of these 7 parameters on the prediction of the corrosion rate of steel bars has not been studied.

Credit Author Statement

Lv Ya-jun: Conceptualization, Methodology, software;
Wang Jun-wei: Data curation, Writing-Original draft preparation;
Wang Julian (Jia-liang): Investigation;
Xiong Cheng: Validation;
Zou Liang, Li-Ly:Writing-Review and Editing;
Li Da-wang:Supervision, Project administration, Funding acquisition.

Declaration of Competing Interest

The authors declare that they have no known competing financial interests or personal relationships that could have appeared to influence the work reported in this paper.

Acknowledgment

The authors gratefully acknowledge the financial supports provided by the National Natural Science Foundation of China (Grants Nos. 51520105012, 51278303, 51779096).

Reference

[1] H. Zhao, K. Jiang, R. Yang, Y. Tang, J. Liu, Experimental and theoretical analysis on coupled effect of hydration, temperature and humidity in early-age cement-based materials, Int J Heat Mass Transf, 146 (2020) 118784.
[2] X. Sun, H. Kong, H. Wang, Z. Zhang, Evaluation of corrosion characteristics and corrosion effects on the mechanical properties of reinforcing steel bars based on three-dimensional scanning, Corros Sci, 142 (2018) 284–94.
[3] Y.G. Du, L.A. Clark, A.H.C. Chan, Residual capacity of corroded reinforcing bars, Mag Concr Res, 57 (3) (2005) 135–47.
[4] H. Husni, M.R. Nazari, H.M. Yee, R. Rohim, A. Yusuff, M.A. Mohd Ariff, N.N.R. Ahmad, C.P. Leo, M.U.M. Junaidi, Superhydrophobic rice husk ash coating on concrete, Constr Build Mater, 144 (2017) 385–91.
[5] D. Li, C. Xiong, T. Huang, R. Wei, N. Han, F. Xing, A simplified constitutive model for corroded steel bars, Constr Build Mater, 186 (2018) 11–19.
[6] M.P. Papadopoulos, C.A. Apostolopoulos, A.D. Zervaki, G.N. Haidemenopoulos, Corrosion of exposed rebars, associated mechanical degradation and correlation with accelerated corrosion tests, Constr Build Mater, 25 (8) (2011) 3367–74.
[7] W. Zhang, X. Song, X. Gu, S. Li, Tensile and fatigue behavior of corroded rebars, Constr Build Mater, 34 (2012) 409–17.
[8] Y. Du, M. Cullen, C. Li, Structural effects of simultaneous loading and reinforcement corrosion on performance of concrete beams, Constr Build Mater, 39 (2013) 148–52.
[9] Y. Du, M. Cullen, C. Li, Structural performance of rc beams under simultaneous loading and reinforcement corrosion, Constr Build Mater, 38 (2013) 472–81.

[10] M.G. Stewart, A. Al-Harthy, Pitting corrosion and structural reliability of corroding rc structures: experimental data and probabilistic analysis, Reliab Eng Syst Saf, 93 (3) (2008) 373–82.
[11] Y.G. Du, L.A. Clarkt, A.H.C. Chan, Effect of corrosion on ductility of reinforcing bars, Mag Concr Res, 57 (7) (2005) 407–19.
[12] W. Zhu, R. François, D. Coronelli, D. Cleland, Effect of corrosion of reinforcement on the mechanical behaviour of highly corroded rc beams, Eng Struct, 56 (2013) 544–54.
[13] W. Zhu, R. François, Experimental investigation of the relationships between residual cross-section shapes and the ductility of corroded bars, Constr Build Mater, 69 (2014) 335–45.
[14] H. Zhao, X. Wu, Y. Huang, P. Zhang, Q. Tian, J. Liu, Investigation of moisture transport in cement-based materials using low-field nuclear magnetic resonance imaging, Mag Concr Resch, 2019;0:1–19.
[15] D. Li, R. Wei, L. Li, X. Guan, X. Mi, Pitting corrosion of reinforcing steel bars in chloride contaminated concrete, Const Build Mater 199 (2019) 359–68.
[16] D. Li, R. Wei, Y. Du, X. Guan, M. Zhou, Measurement methods of geometrical parameters and amount of corrosion of steel bar, Constr Build Mater, 154 (2017) 921–7.
[17] Y. Cheng, A. Hanif, E. Chen, G. Ma, Z. Li, Simulation of a novel capacitive sensor for rebar corrosion detection, Constr Build Mater, 174 (2018) 613–24.
[18] R.C. Sriramadasu, S. Banerjee, Y. Lu, Detection and assessment of pitting corrosion in rebars using scattering of ultrasonic guided waves, NDT & E Int, 101 (2019) 53–61.
[19] K. Dinh, N. Gucunski, T.H. Duong, An algorithm for automatic localization and detection of rebars from gpr data of concrete bridge decks, Autom Constr, 89 (2018) 292–8.
[20] K. Dinh, N. Gucunski, T.H. Duong, Migration-based automated rebar picking for condition assessment of concrete bridge decks with ground penetrating radar, NDT & E Int, 98 (2018) 45–54.
[21] B. Dong, G. Shi, P. Dong, W. Ding, X. Teng, S. Qin, Y. Liu, F. Xing, S. Hong, Visualized tracing of rebar corrosion evolution in concrete with x-ray microcomputed tomography method, Cement Concret Compos 92 (2018) 102–9.
[22] S. Muralidharan, K. Dillistone, J.-.H. Shin, The gulf coast oil spill: extending the theory of image restoration discourse to the realm of social media and beyond petroleum, Public Relat Rev 37 (3) (2011) 226–32.
[23] Z. Deng, H. Sun, S. Zhou, J. Zhao, L. Lei, H. Zou, Multi-scale object detection in remote sensing imagery with convolutional neural networks, ISPRS J Photogramm Remote Sens, 145 (2018) 3–22.
[24] S. Wang, D. Quan, X. Liang, M. Ning, Y. Guo, L. Jiao, A deep learning framework for remote sensing image registration, ISPRS JPhotogramm Remote Sens, 145 (2018) 148–64.
[25] H. Xue, H. Cui, Research on image restoration algorithms based on bp neural network, J Vis Commun Image Represent, 2019;59:204–9.
[26] H. Zhi, S. Liu, Face recognition based on genetic algorithm, J Vis Commun Image Represent, 58 (2019) 495–502.
[27] A. Cencerrado, A. Cortés, T. Margalef, Genetic algorithm characterization for the quality assessment of forest fire spread prediction, Procedia Comput Sci, 9 (2012) 312–20.
[28] C.-.C. Wu, W.-.L. Lee, Y.-.C. Chen, C.-.H. Lai, K.-.S. Hsieh, Ultrasonic liver tissue characterization by feature fusion, Expert Syst Appl, 39 (10) (2012) 9389–97.
[29] A. Bousselham, O. Bouattane, M. Youssfi, A. Raihani, 3D brain tumor localization and parameter estimation using thermographic approach on gpU, J Therm. Biol, 71 (2018) 52–61.
[30] P. Cai, Y. Cai, I. Chandrasekaran, J. Zheng, Parallel genetic algorithm based automatic path planning for crane lifting in complex environments, Autom Constr, 62 (2016) 133–47.
[31] S. Tsantis, D. Cavouras, I. Kalatzis, N. Piliouras, N. Dimitropoulos, G. Nikiforidis, Development of a support vector machine-based image analysis system for assessing the thyroid nodule malignancy risk on ultrasound, Ultrasound Med Biol, 31 (11) (2005) 1451–9.
[32] C.-.S. Lo, C.-.M. Wang, Support vector machine for breast mr image classification, Comput Math Appl, 64 (5) (2012) 1153–62.
[33] N.N. Bhat, K. Kumari, S. Dutta, S.K. Pal, S. Pal, Friction stir weld classification by applying wavelet analysis and support vector machine on weld surface images, J Manuf Process, 20 (2015) 274–81.
[34] H. Gong, Y. Sun, X. Shu, B. Huang, Use of random forests regression for predicting iri of asphalt pavements, Constr Build Mater, 189 (2018) 890–7.
[35] D. Li, R. Wei, F. Xing, L. Sui, Y. Zhou, W. Wang, Influence of non-uniform corrosion of steel bars on the seismic behavior of reinforced concrete columns, Constr Build Mater, 167 (2018) 20–32.
[36] F. Tang, L. Adam, B. Si, Group feature selection with multiclass support vector machine, Neurocomputing, 317 (2018) 42–49.
[37] C. Cortes, V. Vapnik, Support-vector networks, Mach Learn, 20 (3) (1995) 273–97.
[38] Z. Wang, Y.-.H. Shao, L. Bai, C.-.N. Li, L.-.M. Liu, N.-.Y. Deng, Insensitive stochastic gradient twin support vector machines for large scale problems, Inf Sci, 462 (2018) 114–31.
[39] A. Yang, W. Li, X. Yang, Short-term electricity load forecasting based on feature selection and least squares support vector machines, Knowl Based Syst, 163 (2019) 159–73.
[40] C. Lei, J. Deng, K. Cao, Y. Xiao, L. Ma, W. Wang, T. Ma, C. Shu, A comparison of random forest and support vector machine approaches to predict coal spontaneous combustion in gob, Fuel, 239 (2019) 297–311.
[41] S.-w. Fei, M.-J. Wang, Y.-b. Miao, J. Tu, C.-l. Liu, Particle swarm optimization-based support vector machine for forecasting dissolved gases content in power transformer oil, Energy Convers Manag, 50 (6) (2009) 1604–9.
[42] O. Dahhani, A. El-Jouni, I. Boumhidi, Assessment and control of wind turbine by support vector machines, Sustain Energy Technol Assess, 27 (2018) 167–79.
[43] A. Baghban, M. Bahadori, A.S. Lemraski, A. Bahadori, Prediction of solubility of ammonia in liquid electrolytes using least square support vector machines, Ain Shams Eng J, 9 (4) (2018) 1303–12.
[44] C.J.C. Burges, A tutorial on support vector machines for pattern recognition, Data Min Knowl Discov, 2 (2) (1998) 121–67.
[45] G. Cao, L. Wu, Support vector regression with fruit fly optimization algorithm for seasonal electricity consumption forecasting, Energy, 115 (2016) 734–45.
[46] H. Shi, S. Liu, H. Wu, R. Li, S. Liu, N. Kwok, Y. Peng, Oscillatory particle swarm optimizer, Appl Soft Comput, 73 (2018) 316–27.
[47] H. Marouani, Y. Fouad, Particle swarm optimization performance for fitting of Lévy noise data, Phys A: Stat Mech Appl, 514 (2019) 708–14.
[48] A. Lin, W. Sun, H. Yu, G. Wu, H. Tang, Global genetic learning particle swarm optimization with diversity enhancement by ring topology, Swarm Evol Comput, 44 (2019) 571–83.
[49] Y. Wu, Y. Wu, X. Liu, Couple-based particle swarm optimization for short-term hydrothermal scheduling, Appl Soft Comput, 74 (2019) 440–50.
[50] K. Zhang, Q. Huang, Y. Zhang, Enhancing comprehensive learning particle swarm optimization with local optima topology, Inf Sci, 471 (2019) 1–18.
[51] H. Chen, Z. Liu, K. Cai, L. Xu, A. Chen, Grid search parametric optimization for ft-nir quantitative analysis of solid soluble content in strawberry samples, Vib Spectrosc, 94 (2018) 7–15.
[52] S. Shamshirband, M. Tabatabaei, M. Aghbashlo, P.L. Yee, D. Petković, Support vector machine-based exergetic modelling of a di diesel engine running on biodiesel–diesel blends containing expanded polystyrene, Appl Therm Eng, 94 (2016) 727–47.
[53] L. Cao, C. Tu, P. Hu, S. Liu. Influence of solid particle erosion (SPE) on safety and economy of steam turbines. Appl Therm Eng, 150 (2019) 552–63.
[54] C. Mi, Y. Shen, W.J. Mi, Y.F. Huang, Ship identification algorithm based on 3D point cloud for automated ship loaders, J Coast Res, 2015;73(sp1):28–34.
[55] N. Zhao, M. Xia, W. Mi. Modeling and solution for inbound container storage assignment problem in dual cycling mode. Discret Contin Dyn Syst – S. 2020.